Additives Control the Stability of Amorphous Calcium Carbonate via Two Different Mechanisms: Surface Adsorption versus Bulk Incorporation

Zhaoyong Zou,* Xiaofei Yang, Marie Albéric, Tobias Heil, Qihang Wang, Boaz Pokroy, Yael Politi, and Luca Bertinetti*

The mechanisms by which organisms control the stability of amorphous calcium carbonate (ACC) are yet not fully understood. Previous studies have shown that the intrinsic properties of ACC and its environment are critical in determining ACC stability. Here, the question, what is the effect of bulk incorporation versus surface adsorption of additives on the stability of synthetic ACC, is addressed. Using a wide range of in situ characterization techniques, it is shown that surface adsorption of poly(Aspartic acid) (pAsp) has a much larger stabilization effect than bulk incorporation of pAsp and only 1.5% pAsp could dramatically increase the crystallization temperature from 141 to 350 °C. On the contrary, surface adsorption of PO_4^{3-} ions and OH^- ions does not effectively stabilize ACC. However, bulk incorporation of these ions could significantly improve the ACC stability. It is concluded that the stabilization mechanism of pAsp is entirely different from that of PO_4^{3-} and OH^- ions: while pAsp is effectively inhibiting calcite nucleation at the surface of ACC particle, the latter acts to modify the ion mobility and delay crystal propagation. Thus, new insights on controlling the stability and crystallization processes of metastable amorphous materials are provided.

1. Introduction

Amorphous calcium carbonate (ACC) is widely known as a metastable precursor for the formation of crystalline biominerals with unique morphologies and remarkable properties.[1]

Recently, ACC was also used to synthesize a kinetically trapped mineral phase, calcium carbonate hemihydrate, that cannot be otherwise achieved.[2] While ACC crystallizes within minutes under ambient conditions, organisms can control its stability and crystallization pathways.[3] In some organisms ACC can be stabilized for many years.[4] Previous studies have shown that the high stability of biogenic ACC could be attributed to the presence of soluble inorganic and organic additives, such as magnesium (Mg^{2+}) ions,[5] strontium (Sr^{2+}) ions,[6] silicate (SiO_4^-) ions,[7] phosphate (PO_4^{3-}) ions, [4,8] organic molecules,[9] phosphorylated proteins,[8a] and intrinsically disordered proteins,[10] etc. Because crystallization of ACC in solution typically proceeds via a dissolution and recrystallization mechanism,[11] the high stability of ACC in the presence of additives is often ascribed to their ability to inhibit the dissolution of ACC or the formation of crystalline phases.[5a,12] Furthermore, biogenic ACC was suggested to crystallize mainly via a solid-state transformation mechanism due to the absence of bulk water,[13] however, how additives affect the crystallization mechanisms of ACC in the absence of bulk water is not well understood.

Prof. Z. Zou, Dr. M. Albéric, Prof. Y. Politi, Dr. L. Bertinetti
Department of Biomaterials
Max Planck Institute of Colloids and Interfaces
Potsdam 14476, Germany
E-mail: zzou@whut.edu.cn; Luca.Bertinetti@mpikg.mpg.de
Prof. Z. Zou, Q. Wang
State Key Laboratory of Advanced Technology for Materials
Synthesis and Processing
Wuhan University of Technology
Wuhan 430070, China

Prof. X. Yang
College of Science
Institute of Materials Physics and Chemistry
Nanjing Forestry University
Nanjing 210037, China
Dr. M. Albéric
Sorbonne Université
CNRS
Laboratoire Chimie de la Matière Condensée de Paris
Paris 75005, France
Dr. T. Heil
Department of Colloid Chemisty
Max Planck Institute of Colloids and Interfaces
Potsdam 14476, Germany
Prof. B. Pokroy
Department of Materials Science and Engineering
Technion-Israel Institute of Technology
Haifa 32000, Israel
Prof. Y. Politi, Dr. L. Bertinetti
B CUBE - Center for Molecular Bioengineering
Technische Universität Dresden
Dresden 01307, Germany

**ADVANCED
SCIENCE NEWS**

www.advancedsciencenews.com

**ADVANCED
FUNCTIONAL
MATERIALS**

www.afm-journal.de

The crystallization temperature of ACC under heating varies significantly from ≈130 to 350 °C depending on the preparation method,[14] pH,[15] particle size,[11] water content[16] and the presence of additives.[7a,16b,17] It has been previously suggested that the crystallization of ACC under heating is initiated by a nucleation event that starts from the surface and that the bulk of the ACC particle then crystallizes by a solid-state transformation.[13c,d,18] At room temperature, the crystallization of ACC in air strongly depends on the relative humidity and an interface-coupled dissolution/reprecipitation mechanism was suggested.[19] These studies suggest that the surface structure of ACC is important for its stability. Therefore, to understand the stabilization mechanisms of additives, it is critical to distinguish between the cases in which the additives act on the surface and when they act from within the bulk of the ACC particle.

In this study, we investigated the influence of the localization of additives like poly(Aspartic acid) (pAsp), PO_4^{3-} ions and OH^- ions on the stability of ACC under heating in air. pAsp and PO_4^{3-} ions are common additives used to stabilize ACC in solution and it has been shown that ACC synthesized at higher pH is more stable than that obtained at lower pH[15] likely due to the incorporation of OH^- ions in the mineral. All additives were either incorporated in the ACC bulk by co-precipitation or adsorbed on the surface of the ACC spheres by addition post precipitation. We followed the structural evolution during crystallization by various in situ characterization techniques, such as thermogravimetric analysis/differential scanning calorimetry (TGA/DSC), wide angle X-ray scattering (WAXS), pair distribution function analysis (PDF), and infrared spectroscopy. We first present and discuss the effect of pAsp on the stability of ACC and then compare it with the effect of inorganic anions: OH^- and PO_4^{3-} ions. Results show that the mechanisms by which additives stabilize ACC strongly depend on the characters of the additives and their spatial distribution within the nanoparticles. Thus, new insights on controlling the stability of amorphous materials are provided and our study also provides valuable inspirations for material scientists to design strategies to improve the stability of unstable functional materials.

2. Results and Discussion

2.1. Influence of pAsp Localization on the Stability of ACC

2.1.1. Synthesis and Characterization of the Different ACC Samples

Pure ACC (ACC-0%) was synthesized by adding 0.5 mL of 1 M $CaCl_2$ solution into 49.5 mL of 10.1×10^{-3} M Na_2CO_3 solution at a rate of 10 mL min^{-1}. In accordance with previous studies,[12a,20] pAsp incorporation in the bulk of ACC was achieved by adding different amounts of 1 mg mL^{-1} pAsp aqueous solution to the Na_2CO_3 solution before the addition of $CaCl_2$. These samples are hereafter referred to as ACC$_B$-x%, where x% represents the initial molar ratio of the amino acid monomer to calcium ions. ACC with pAsp adsorbed on the surface was prepared by adding the same pAsp aqueous solution 10 s after the precipitation of pure ACC and the samples were named as ACC$_S$-x%. Detailed experimental parameters are summarized in **Table 1**.

In our previous studies,[11,20] we have shown that the average particle size of pure ACC synthesized under the same condition was 120 ± 40 nm, and pAsp could significantly reduce the particle size of ACC to 74 ± 30 nm even in the presence of only 0.3% pAsp due to a cooperative ion-association process.[20] The the particle size of ACC synthesized in the presence of 1.5% pAsp, corresponding to ACC$_B$-1.5%, was similar to that of 0.3% pAsp. Here, the average particle size of ACC$_B$-3% calculated from the scanning electron microscopy (SEM) images (**Figure 1**A) was 75 ± 25 nm, indicating no significant differences in the particle size of all ACC$_B$-x% samples. For ACC$_S$-x%, post addition of pAsp after the formation of ACC has little effect on the particle size of ACC[12a] and the average particle size of ACC$_S$-3% sample calculated from the SEM image (Figure 1B) was 121 ± 25 nm, which is similar to that of pure ACC. Infrared spectra of all samples (Figure S1, Supporting Information) were almost identical presenting the typical vibrations bands of ACC. Raman spectra also confirmed that all samples were amorphous (Figure 1C), with characteristic bands at 210, 702, 725, and 1082 cm^{-1}.[11,21] It should be noted that the slightly lower value for the Raman lines as compared to our previous study (214, 727, and 1084 cm^{-1}) likely results from the use of a high-resolution grating of 1800 g mm^{-1} with respect to previously reported results.[11] In addition, the appearance of the C-H vibrational peaks from 2800–3200 cm^{-1} in the Raman spectra of ACC$_B$-3% and ACC$_S$-3% indicated the presence of pAsp in these samples. According to the relative intensity of these peaks to the carbonate peak at 1082 cm^{-1}, the amount of pAsp in ACC$_B$-3% was higher than that in ACC$_S$-3%.

The total amount of pAsp incorporated within the ACC samples was obtained from amino acid analysis (AAA). Results (Table 1) showed that the Asp/Ca bulk molar ratio in all ACC$_B$-x% samples was similar to the corresponding initial value in the solution. Based on the concentration of Ca^{2+} ions in the solution after ACC formation (1×10^{-3} M) we calculated that nearly 80% of the pAsp was incorporated in ACC nanoparticles. However, in all ACC$_S$-x% samples, independently of the initial pAsp concentration, the Asp/Ca bulk molar ratio was maintained at ≈1%. As pAsp molecules were added after the formation of ACC, having similar particle size and agglomeration state, it could only be adsorbed on the surface of ACC nanoparticles leading to a constant incorporation value around 1%. To probe the content of pAsp on the surface of ACC nanoparticles, surface sensitive X-ray photoelectron spectroscopy (XPS) analysis was performed. Results (Table 1) showed that the Asp/Ca surface molar ratio within a depth of ≈10 nm from the surface reached 36% for ACC$_S$-3%, which is locally ≈1.5 times higher than that of ACC$_B$-3% (25%). Similarly, the value for ACC$_S$-0.75% (23%) was locally ≈2 times higher than that of ACC$_B$-0.75% (12%).

Previous studies have shown that the incorporation of organic molecules in the crystal of calcite or aragonite causes lattice distortions, which can be detected by high-resolution X-ray diffraction (HRXRD).[22] Therefore, the incorporation of pAsp in ACC samples was further investigated by heating the samples to 500 °C and characterizing the crystallization products by both laboratory XRD and HRXRD at the ID22 powder X-ray diffraction beam line at the European Synchrotron Research Facility (ESRF). The results (Figures S2 and S3,

Table 1. Experimental conditions, the amino acid to Ca molar ratio obtained from amino acid analysis (AAA) and X-ray photoelectron spectroscopy (XPS) and the crystallization temperature for the different samples.

Sample name	Addition of pAsp	Initial Asp/Ca/M/M	Asp/Ca total[a]/M/M	Asp/Ca surface[a]/M/M	Crystallization T [°C]
ACC-0%	–	0%	0%	0%	141
ACC$_S$-0.75%	After ACC	0.75%	1.0%	23.3%	275
ACC$_S$-1.5%	After ACC	1.5%	1.1%	–	350
ACC$_S$-3%	After ACC	3%	0.9%	36.0%	357
ACC$_B$-0.75%	Before ACC	0.75%	0.9%	12.2%	249
ACC$_B$-1.5%	Before ACC	1.5%	1.5%	–	265
ACC$_B$-3%	Before ACC	3%	2.6%	24.7%	286

[a]The total Asp/Ca molar ratio was measured by AAA and the value on the surface was obtained from XPS analysis.

Supporting Information) show that all ACC samples crystallized to calcite after crystallization. No differences can be observed between crystallized ACC-0% and crystallized ACC$_S$-x% in terms of peak position and width (**Figure 2**), however, pronounced peak-shifts and broadening of all diffraction peaks were observed for the crystallization product of the ACC$_B$-x% samples (Figure S3 (Supporting Information) and Figure 2). The calcite lattice parameters were calculated by Rietveld refinement (Figure S4, Supporting Information). The c-lattice parameter showed an expansion for ACC$_B$-3% as compared to ACC-0% as evidenced by a shift of the 006 peak to larger d-spacing ($\Delta d/d = 7.9 \times 10^{-4}$), while the a- and b-lattice parameters showed shrinkage evidenced by a shift to lower d-spacing for the 012 peak ($\Delta d/d = -8.4 \times 10^{-4}$), the 104 peak ($\Delta d/d = -2.2 \times 10^{-4}$), and the 110 peak ($\Delta d/d = -1.3 \times 10^{-3}$). These observations are similar to those reported for biogenic calcite crystals[22c] and synthetic calcite incorporating amino acids.[22a] The broadening of the diffraction peaks is typically ascribed to the decrease of the size of coherently scattering crystalline blocks and / or the increase of the microstrain fluctuations,[22c] due to the smaller particle size of ACC and the degradation of intra-crystalline organic macromolecules upon mild annealing treatments. These results, together with the AAA and XPS data, confirm that pAsp molecules were mostly incorporated in the bulk of ACC$_B$-x% nanoparticles, whereas for ACC$_S$-x% samples they were present mainly at the surface of the nanoparticles.

2.1.2. Stability of the pAsp ACC samples under Heating

The thermal stability and crystallization behavior of the ACC samples were investigated by TGA/DSC, at a heating rate of 3 °C min^{-1} (**Figure 3**A–D). As shown in Figure 3A, the crystallization temperature of ACC increased dramatically from 141 °C for ACC-0% to 249 °C for ACC$_B$-0.75% and reached 286 °C for ACC$_B$-3%. It suggests that even a small amount of pAsp incorporated in the bulk could significantly stabilize the amorphous phase. More strikingly, however, are the remarkably higher crystallization temperatures of the ACC$_S$-x% samples than the ones of the corresponding ACC$_B$-x% samples (Figure 3B). For example, ACC$_S$-3% remained stable until 357 °C whereas ACC$_B$-3% crystallizes at 286 °C. Interestingly, an almost linear increase of the crystallization temperature with respect to the surface Asp/Ca molar ratio was obtained (Figure 3E), regardless of the total amount of pAsp in the bulk.

The TGA curves (Figure 3C,D) show that, although the fraction of water in all samples varied in the range from 12% to
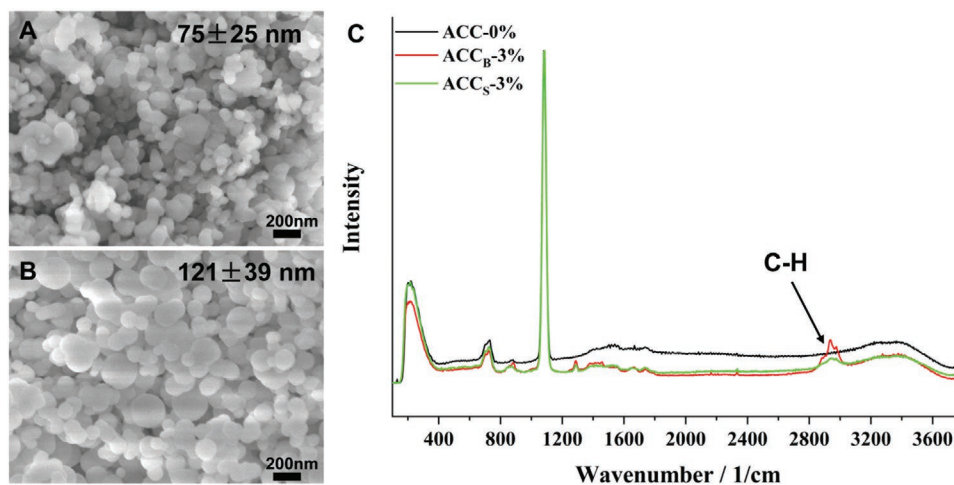

Figure 1. SEM images of A) ACC$_B$-3%, B) ACC$_S$-3%, and C) Raman spectra of pure ACC (ACC-0%, black color), ACC$_B$-3% (red color), and ACC$_S$-3% (green color).
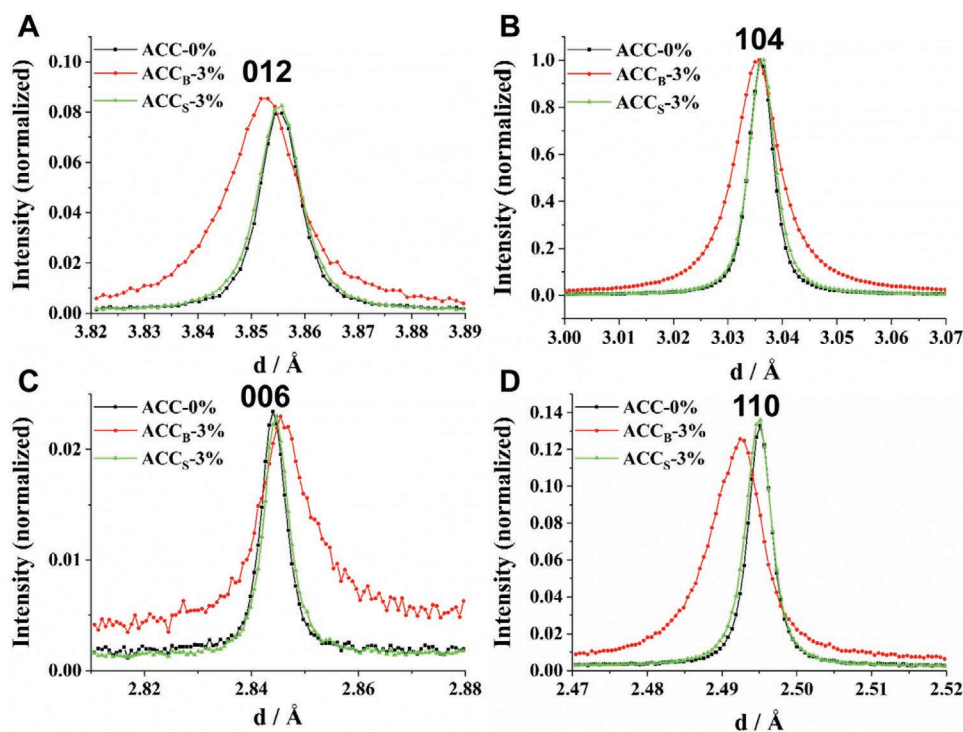
Figure 2. Selected high resolution diffraction peaks taken from crystallization products of ACC (black color), ACC$_B$-3% (red color), and ACC$_S$-3% (green color) after heating to 500 °C at 3 °C min^{-1}: A) 012 peak, B) 104 peak, C) 006 peak, and D) 110 peak.

17%, the differences could be related to loosely bound mobile H_2O which are released before 130 °C. These variations did not correlate with the thermal stability of ACC. This is consistent with previous studies showing that the total H_2O content does not correlate with crystallization temperature.[14a,15a]

To quantify the contribution of pAsp to the stabilization of ACC, we performed a series of TGA/DSC analyses for ACC$_S$-3% at different heating rates from 1.5 to 10 °C min^{-1} (Figure 3F,G). DSC curves (Figure 3F) showed that the crystallization temperature increased with increasing heating rate reaching 374 °C at 10 °C min^{-1}. The apparent activation energies for ACC crystallization were then derived using standard methods (Figure S5, Supporting Information).[23] For pure ACC, a value of 87 kJ mol^{-1} was obtained, which can be compared with reported values of 100[18] and 73 kJ mol^{-1} [24] for ACC without additives. For ACC$_S$-3%, the activation energy increased to ≈225 kJ mol^{-1}, which is similar to that of ACC synthesized at high pH (12.5).[15b] Interestingly, TGA curves of ACC$_S$-3% (Figure 3G) showed a clear weight loss concurrent with the sharp exothermal peak on DSC curves (Figure 3F), especially at higher heating rates. This weight loss could be attributed to the decomposition of pAsp starting from ≈340 °C.[17] Indeed, integration of the exothermic peak for pure ACC reveals that the enthalpy of crystallization is −13 kJ mol^{-1}. However, the enthalpy of the peak for ACC$_S$-3% is −21 kJ mol^{-1}, confirming that the enthalpy contains contribution not only from ACC crystallization, but also from the decomposition of pAsp. These results suggest that the decomposition of pAsp triggers the nucleation of calcite from the surface of ACC nanoparticles.

2.1.3. In Situ Structural Characterization of the Crystallization Process

To gain a better understanding of the crystallization process, in situ wide angle X-ray scattering (WAXS) analysis was performed at the μspot beamline at BESSY, Berlin. As shown in **Figure 4**A and Figure S6 (Supporting Information), the onset of calcite formation can be clearly determined from the appearance of the 104 peak, which corresponds well to the crystallization temperature obtained from TGA/DSC analysis. The crystallization degree can be deduced from the integrated area of the 104 peak and the crystallization rate can be extracted from the slope of the curves (Figure 4B). For ACC-0%, the integrated area increased quickly and reached a plateau at 170 °C, suggesting that, at this temperature, all ACC transformed into calcite. For the ACC$_B$-3% sample, the integrated area increased slowly after the onset of the crystallization (at 285 °C) and reached the plateau at 360 °C. Although ACC$_S$-3% crystallized at higher temperature than ACC$_B$-3%, it showed similar crystallization rate. These results suggest that the localization of pAsp in ACC has little influence on the crystallization kinetics of ACC.

In situ PDF analysis was used to investigate the local structural changes upon dehydration and crystallization of the different ACC samples during heating. The PDF analysis is especially sensitive to local structure of Ca atom. At room temperature, the peak positions are similar to those reported in literature,[16b,25] but we observed a small change in the intensity of all peaks for ACC$_B$ as compared to ACC$_S$ and pure ACC (Figure S7, Supporting Information). Despite this minor difference, the evolution of the local structure during in situ heating were quite similar. Taken ACC$_S$-3% for example (**Figure 5**A,B),
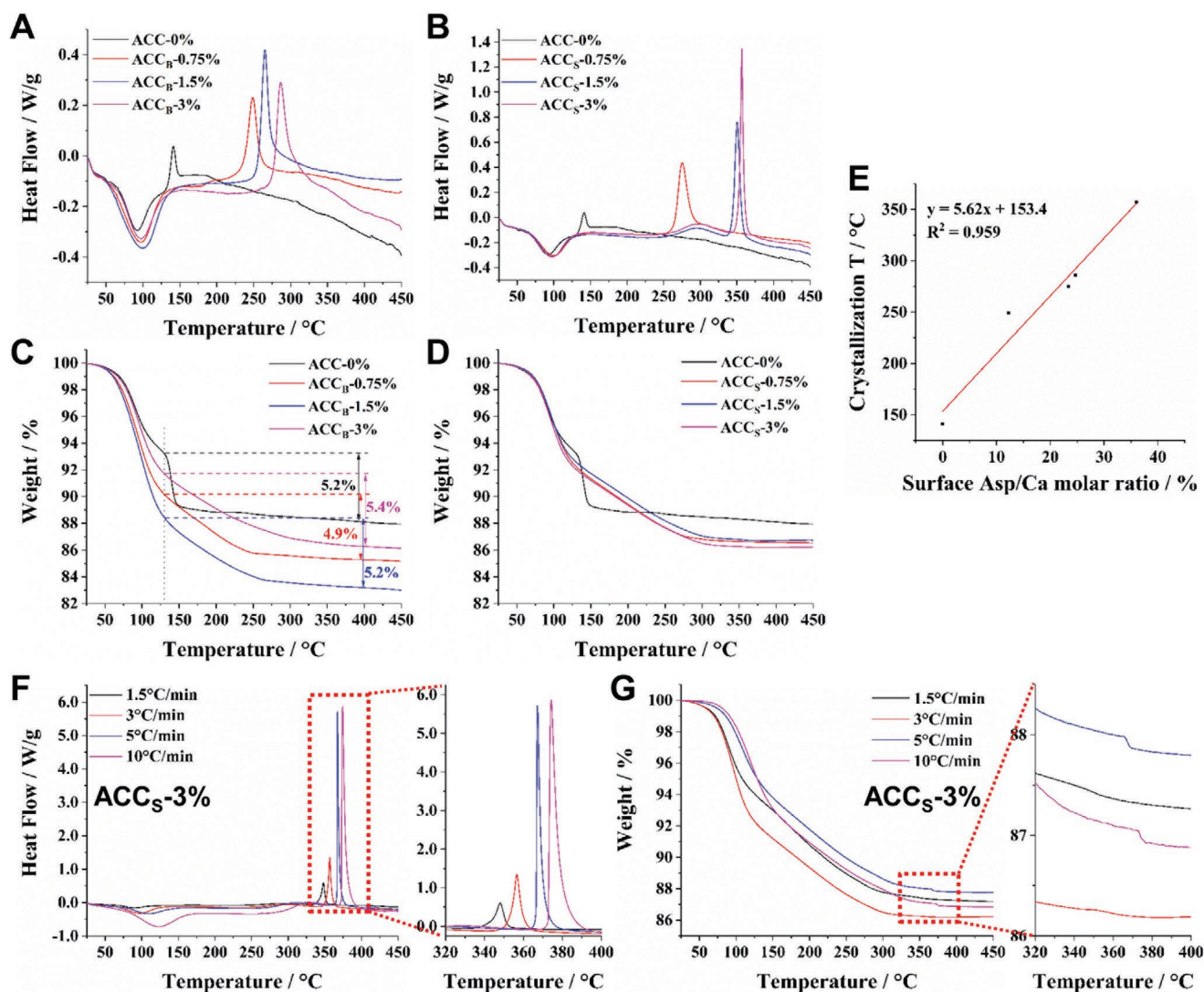
Figure 3. DSC A–B) and TGA C–D) curves of ACC_B-x% A, C) and ACC_S-x% B, D) at a heating rate of 3 °C min^{-1}. E) The crystallization temperature of different ACC samples versus their Asp/Ca molar ratio on the surface (from XPS analysis) and a linear fit of the data (red solid line). DSC F) and TGA G) curves of ACC_S-3% at different heating rates. Insets in (F) and (G) show the zoom-in from 320 to 400 °C (marked by red dashed rectangles), respectively. The differences marked on TGA curves in C) represent the amount of restrictedly mobile water and rigid structural water that are removed after heating to 130 °C.

the peak at 2.4 Å (mainly originating from Ca-O pairs[16b,25]) shifted to lower distances during the dehydration step for temperatures up to 100 °C. At the same time, a peak at ≈4.0 Å appeared and its intensity increased. Afterward, the intensity of the peak at 2.9 Å gradually decreased and the intensity of the peak at 4.1 Å (from Ca-O and Ca-Ca pairs[16b]) increased until the crystallization of ACC. These results indicate that short-range structural rearrangement occurred throughout the dehydration process and until the onset of ACC crystallization involving the removal of structural water.[16b]

To probe the change of the local environment of carbonate group (CO_3^{2-}), we used in situ infrared analysis under heating. For the ACC_S-3% (Figure 5C,D), the onset of ACC crystallization can be indicated by the decreasing intensity of the ν1, ν2, and ν4 peaks of ACC and the appearance of characteristic calcite

peaks at 713 (ν4) and 875 (ν2) cm^{-1}. Similar to the PDF analysis, there was also a small change in local environment during dehydration and before crystallization, indicated by the shift of ν2 peak from 863 to 860 cm^{-1} originating from an intensity increase at 860 cm^{-1}. The symmetric stretch (ν1) was broadened and its intensity increased slightly. The broadening of these vibrational bands was also observed in ex situ measurements of infrared spectra collected at room temperature before and after heating to 300 and 500 °C (Figure S8, Supporting Information). Similar observations were reported by Gal et al.,[7a] but they are in contrast to those reported by Ihli et al.,[18] where a reduction in intensity of the ν1 absorption band and a slight shift in the ν2 band to higher frequencies were observed during the dehydration of ACC and before the detection of any crystalline phases. Although the origin for the different changes in the
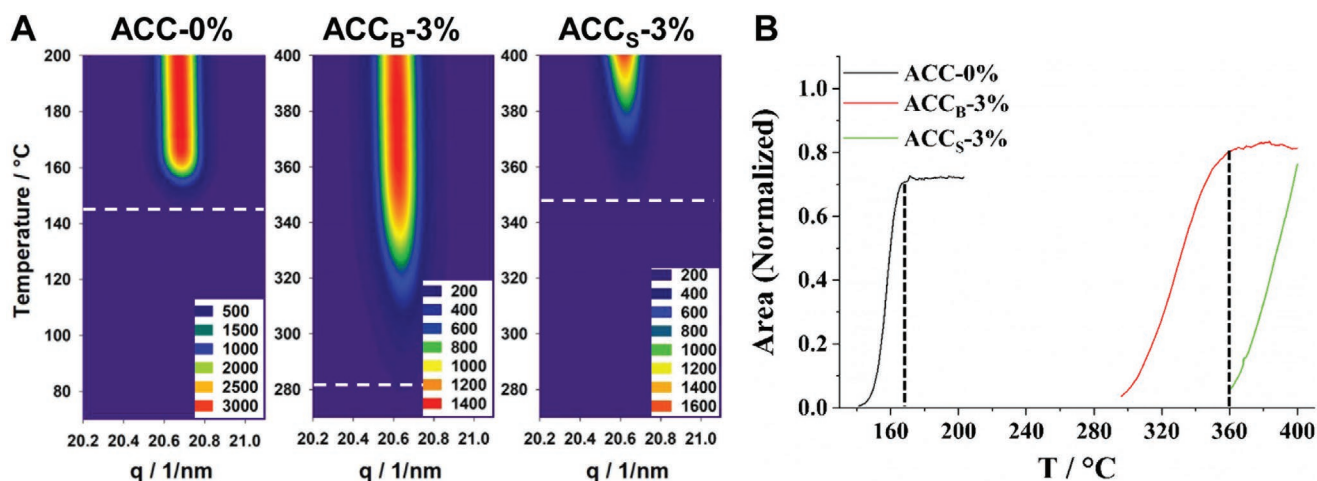
**ADVANCED
SCIENCE NEWS**

www.advancedsciencenews.com

**ADVANCED
FUNCTIONAL
MATERIALS**

www.afm-journal.de

Figure 4. Synchrotron in situ WAXS analysis (μspot, $\lambda = 0.82656$ Å) of ACC-0%, ACC_B-3%, and ACC_S-3% during heating at 3 °C min^{-1}. Contour plot of the 104 peak of different samples A), evolution of the normalized area B) of the 104 peak of different samples. Dashed lines in A) represent the temperature at which the 104 peak appears. Dashed line in B) indicated the temperature at which ACC transformation nearly completed.

spectral features is not clear, our data clearly demonstrates the local structural changes of ACC during dehydration and before crystallization. In addition, in situ infrared analysis was also performed for sample ACC_B-3% and no significant differences could be detected between ACC_B-3% (Figure S9, Supporting Information) and ACC_S-3% (Figure 5C,D), suggesting that the observed local structural changes do not depend on the presence of pAsp.

TEM image and selected area electron diffraction (SAED) pattern of ACC_S-3% confirmed that the spherical nanoparticles
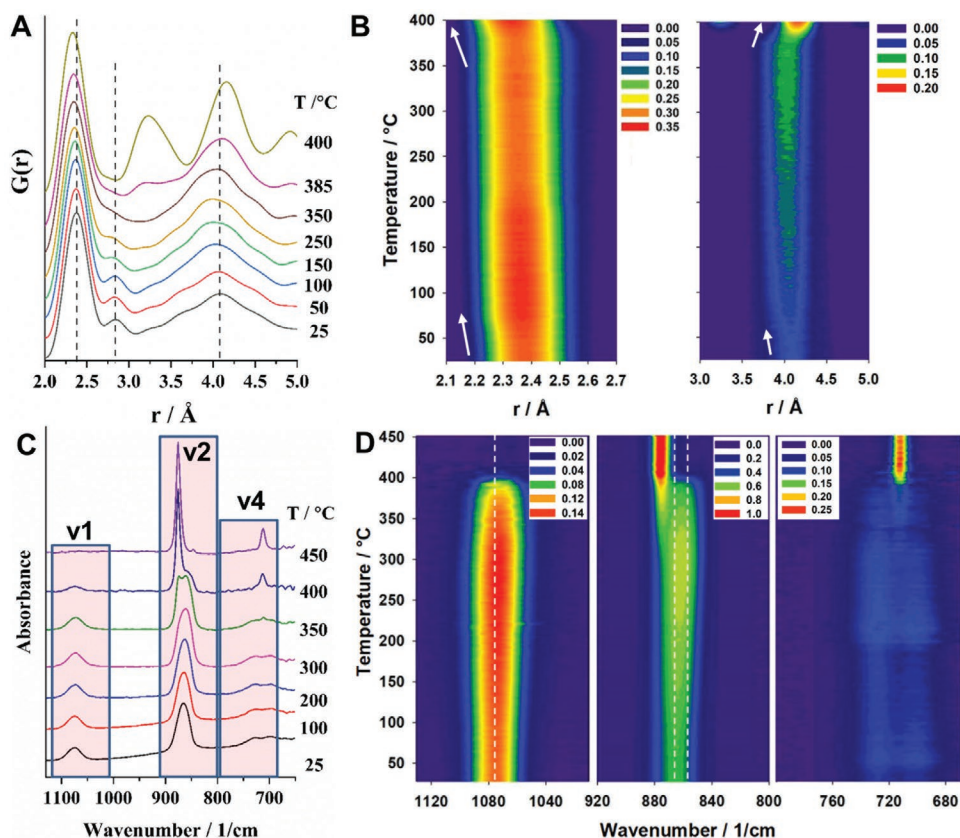

Figure 5. PDF patterns A) of ACC_S-3% at different temperatures during in situ heating at 3 °C min^{-1} and corresponding contour plots B). White arrows indicate the shifts of the peaks. FTIR C) spectra of ACC_S-3% at different temperatures during in situ heating at 3 °C min^{-1} and the corresponding contour plot D) of different bands after background subtraction. Black dashed lines in D) are used to better visualize the evolution of the peaks.
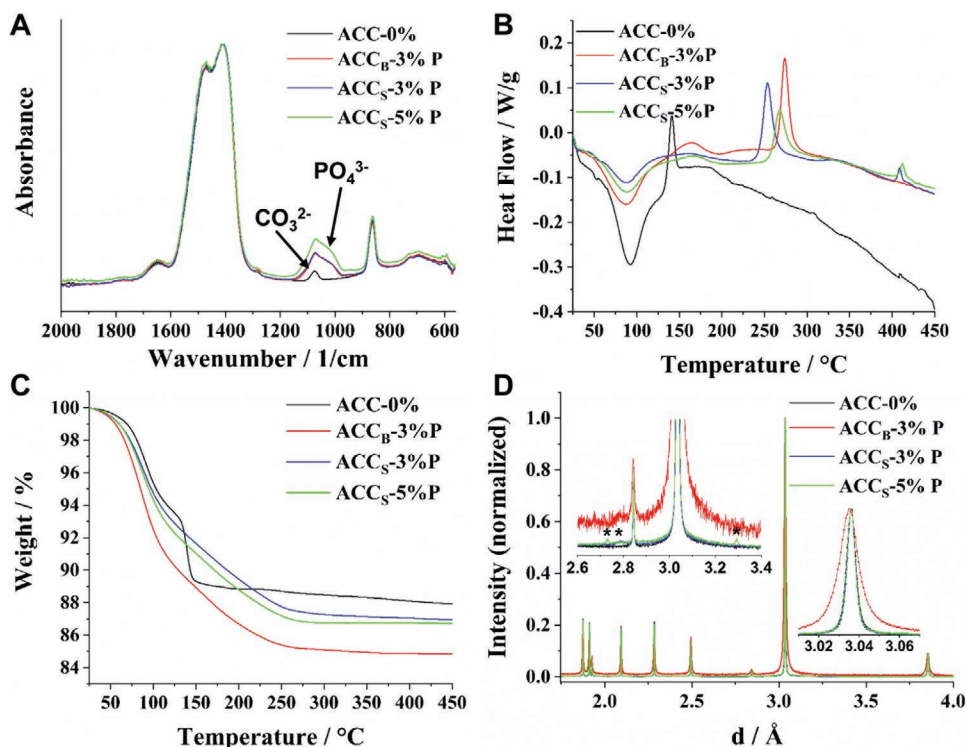
**ADVANCED
SCIENCE NEWS**
www.advancedsciencenews.com

**ADVANCED
FUNCTIONAL
MATERIALS**
www.afm-journal.de

Figure 6. FTIR spectra A) of ACC-0%, ACC$_B$-3%P, ACC$_S$-3%P and ACC$_S$-5%P. DSC B) and TGA C) curves of ACC-0%, ACC$_B$-3%P, ACC$_S$-3%P and ACC$_S$-5%P. HRXRD patterns D) of the samples after heating to 500 °C. Insets in B) are magnified regions of the HRXRD patterns and the * symbol indicated the presence of weak peaks.

were amorphous (Figure S10A,B, Supporting Information). After heat-induced crystallization (Figure S10C–J, Supporting Information), no significant changes in the morphology could be distinguished, but each nanoparticle transformed into a single crystal of calcite, as observed in previous studies. [9b,26]

2.2. Influence of Anionic Inorganic Additives Localization on the Stability of ACC

Besides pAsp, inorganic anions like phosphate (PO_4^{3-}) ions have also been shown to stabilize ACC.[4,8,16b] Therefore, using similar methods, we synthesized ACC with PO_4^{3-} ions either incorporated in the bulk (ACC$_B$-3%P) or adsorbed on the surface (ACC$_S$-3%P and ACC$_S$-5%P). In situ pH and Ca^{2+} activity measurements of the reaction solutions (Figure S11, Supporting Information) showed that both the pH and Ca^{2+} activity decreased significantly after the addition of PO_4^{3-} ions, suggesting the precipitation of amorphous calcium phosphate (ACP) through the complexation of PO_4^{3-} ions with the Ca^{2+} ions in solution. Infrared spectra (**Figure 6**A) confirmed the successful incorporation of PO_4^{3-} ions in all samples and their total amounts in ACC$_B$-3%P and ACC$_S$-3%P were similar. TGA/DSC results (Figure 6B,C) showed that the crystallization temperature increased significantly if the surface of ACC nanoparticles were modified by PO_4^{3-} ions, confirming the importance of surface PO_4^{3-} ions in stabilizing ACC. However, unlike pAsp, PO_4^{3-} ions in the bulk could further stabilize ACC, and ACC$_B$-3%P was even more stable than ACC$_S$-5%P. In

addition, a small exothermic peak at 420 °C on the DSC curve of ACC$_S$-x%P may be attributed to the crystallization of phosphate containing amorphous phases, suggesting the accumulation of Ca-phosphate on the surface ACC nanoparticles.

HRXRD patterns (Figure 6D) showed that all samples transformed into calcite after heating up to 500 °C. However, there was also a broad peak at a d-spacing of 2.79 Å for ACC$_S$-3%P and two additional peaks at 2.73 and 3.29 Å for ACC$_S$-5%P, which could be ascribed to a crystalline calcium phosphate phase like calcium pyrophosphate.[27] This is consistent with the crystallization peak at 420 °C observed in the DSC curves for ACC$_S$-x%P samples, suggesting that PO_4^{3-} ions were incorporated in the bulk of ACC$_B$-3%P, while they were present on the surface of ACC$_S$-x%P nanoparticles. In addition, the calcite diffraction peaks were almost identical between ACC$_S$-x% and ACC-0%. Although significant peak broadenings were observed for ACC$_B$-3%P, there was no associated shift the peak position, suggesting that the PO_4^{3-} ions are not incorporated inside the calcite lattice after crystallization, but likely force the crystallization into smaller coherent domains. This is consistent with previous studies showing that phosphate is incompatible with calcite structure and that the crystallization of a mixed phase of ACC and ACP leads to separation of these two phase and transformation into calcite and hydroxyapatite, respectively.[8b,28]

Another important factor known to influence the stability of ACC is the presence of OH^- ions (i.e the solution pH). To test the effect of OH^- ions incorporated in the bulk and those adsorbed on the surface, we added 2 mL 1 M sodium hydroxide (NaOH) before (ACC$_B$-OH^-) or after (ACC$_S$-OH^-) the formation

**ADVANCED
SCIENCE NEWS**

www.advancedsciencenews.com

**ADVANCED
FUNCTIONAL
MATERIALS**

www.afm-journal.de

of ACC. The final pH value for the solution in both preparations was 12.3. The crystallization temperature for ACC_B-OH^- was 317 °C (Figure S12, Supporting Information), consistent with literature values.[15a] However, the crystallization temperature for ACC_S-OH^- only increased slightly from 141 to ≈163 °C (Figure S12, Supporting Information). Thus, post addition of OH^- ions is not effective in stabilizing ACC but the incorporation of OH^- in ACC bulk is critical for the high stability of ACC.

A comparison of the effects of different additives on the stability of ACC suggests that the stabilizing mechanisms are different. For the organic additive pAsp, we showed that surface incorporation has a larger effect on the stabilization of ACC relative to its incorporation in the bulk. The temperature of crystallization scales almost linearly with the pAsp to calcium molar ratio on the surface, and crystallization is initiated only when surface pAsp is decomposed. Furthermore we found no kinetic effect on the crystal propagation in the presence of bulk additives. These results are consistent with pAsp inhibition of calcite nucleation at the surface of ACC and little or no effect on calcite propagation.

Contrary to pAsp, the effect of inorganic PO_4^{3-} and OH^- ions is larger when they are incorporated in the bulk rather than when they are adsorbed on the surface of ACC spheres. It is likely that neither anion has a strong effect on the structure and mobility of ions at the surface. According to classical nucleation theory, the nucleation rate strongly depends on the diffusion of ions, a thermally activated process.[29] If the mobility of ions at the surface of ACC nanoparticles is restricted by additives, then the nucleation rate of calcite decrease and the onset of ACC crystallization delayed. A previous study showed that phosphate-containing ACC is stable because dispersion of PO_4^{3-} ions within ACC nanoparticles crystallized after the phase separation of PO_4^{3-} ions and water from the initial homogeneous phase.[8b] Therefore, a possible reason could be that post addition of inorganic ions like PO_4^{3-} ions lead to the formation of individual ACP phase either on the surface of ACC nanoparticles or in solution. When OH^- ions are added after the formation of ACC, the surface of ACC nanoparticle is not likely altered because ion association between Ca^{2+} ions and CO_3^{2-} ions is much stronger than any of them and OH^- ions.[30] Particle size effect is also not relevant as no significant difference with respect to particle size was observed between ACC_B-OH^- and ACC_S-OH^- (Figure S13, Supporting Information).

Surface adsorption of additives has no effect on particle size, but bulk incorporation on the other hand results in significantly smaller ACC particles, which might lead at least partially to the observed stabilization effect.[11] For example, the average particle size of ACC_B-3%P (≈40 nm) is much smaller than ACC_S-x% (≈120 nm). Thus, although anions do not affect the surface properties, they strongly alter the surface to bulk ratio, but more importantly, the addition of inorganic additives strongly affects the mobility of ions through binding to water, hydroxyl ions, and/or Ca^{2+} ions[8b,16b,31] and therefore the propagation of the crystallization.

3. Conclusion

In conclusion, using various in situ characterization techniques, we compared the stabilizing effects of additives incorporated in

the bulk and of additives adsorbed on the surface of ACC nanoparticles. We showed that the effect of pAsp is highest when it is adsorbed on the surface of ACC nanoparticles, however, PO_4^{3-} and OH^- ions are only effectively stabilizing ACC when they are incorporated in the bulk mineral. Therefore, the mechanisms by which additives stabilize ACC strongly depend on the characters of the additives and their spatial distribution within the nanoparticles. While pAsp is effectively inhibiting calcite nucleation at the surface of ACC particle, PO_4^{3-} and OH^- ions act to modify the ion mobility therefore delaying crystal propagation. Furthermore, the observation that the stability of the amorphous phase can be significantly increased by modifying the surface structure with a small amount of polymer opens the possibility to further functionalize the nanoparticles and may have great implications for the application of stable amorphous materials.

4. Experimental Section

Materials and General Preparative Methods: Analytical grade calcium chloride dihydrate ($CaCl_2 \cdot 2H_2O$), sodium carbonate decahydrate ($Na_2CO_3 \cdot 10H_2O$), sodium dihydrogen phosphate (NaH_2PO_4), sodium hydroxide (NaOH) and poly-(α,β)-DL-(aspartic acid sodium salt) (Mw = 2000—11 000 Da) were purchased from Sigma-Adrich without further purification. The calcium solution, carbonate solution, phosphate solution and 1 mg mL^{-1} pAsp solution were prepared by dissolving corresponding chemicals in ultrapure water. Experiments were performed using a computer controlled titration system (905 Titrando, Metrohm Ltd.).

ACC Synthesis and Crystallization in Solution: In a typical experiment, ACC was synthesized by dosing 0.5 mL 1 M calcium solution into the reaction vessel containing 49.5 mL carbonate solution under stirring. A dosing rate of 10 mL per minute was used to ensure a rapid mixing of the two solutions. The concentration ratio of calcium to carbonate after mixing was 1:1. The precipitates were collected immediately after precipitation by fast vacuum filtering of the reaction solution and rinsed with ethanol. The dry powders were then stored in a vacuum desiccator for further characterization. For ACC with additives in the bulk, certain amounts of additive solutions were added in the carbonate solution before ACC precipitation. For ACC with additives on the surface, the additive solutions were added 10 s after the precipitation of ACC.

Scanning Electron Microscopy and Transmission Electron Microscopy: Scanning electron microscopy was performed using a field emission scanning electron microscope (JEOL, JSM-7500F) working at an acceleration energy of 5 keV. Samples were not coated prior to investigation. Transmission electron microscopy and electron diffraction analysis were performed using a Jeol JEM-ARM200F working at 200 kV. Particle size measurements of the SEM images were performed by using the program Fiji.

Thermogravimetric Analysis/Differential Scanning Calorimetry: Thermogravimetric Analysis/Differential Scanning Calorimetry was performed using a SENSYS evo (SETARAM Instrumentation, Caluire, France) from 25–500 °C at a heating rate of 3 °C min^{-1}. Approximately 15 mg of powdered sample was placed in an alumina crucible. The purge gas was dry nitrogen. TGA/DSC experiments were repeated at least 3 times for 0% and 3% pAsp samples and twice for other samples.

High Resolution X-Ray Powder Diffraction: High resolution X-ray powder diffraction (XRD) measurements were performed at the beamline ID22 of the European Synchrotron Radiation Facility (ESRF, Grenoble, France). The X-ray wavelength (0.399952 Å) was calibrated with Si standard sample (NIST, Gaithersburg, MD, USA). The powder samples were put in glass capillaries and measured at room temperature. Rietveld refinement analysis was performed using the FULLPROF program version 2017,[32] with a 6 coefficients polynomial background fitting and a least squares refinement weighting model.

In Situ Wide-Angle X-Ray Scattering: Wide-angle X-ray scattering experiments were carried out at the synchrotron μ-Spot beamline (BESSY II storage ring, Helmholtz-Zentrum Berlin) using a multilayer monochromator and spot size of 100 μm. A MarMosaic CCD detector (Rayonix L.L.C., Evanston, IL, USA) was used to collected 2D scattering patterns in the transmission geometry. The rings of the pattern were circular and the intensity around each ring was uniform. Radial integration of the patterns with the software DADAK gave the spherically averaged scattering intensity as a function of the modulus of the scattering vector q. Here $q = 4\pi \sin(\theta)/\lambda$, 2θ is the scattering angle and λ is the wavelength. Calibration of the beam center, detector tilt angle, detector tilt rotation angle and sample to detector distance was perfomed using the diffraction pattern of Quatz as standard. An additional background signal resulting from the Kapton foil windows of the in situ heating setup (Linkam FTIR600, Linkam Scientific Instruments, Surrey, UK) was also subtracted. The powder samples were mounted on a cylindrical sample holder inside the heating stage. The sample was heated from 25 to 400 °C at a rate of 2 °C min^{-1}.

In Situ Pair Distribution Function Analysis: Pair distribution function (PDF) analysis was performed at the X-PDF station (I15-1) in Diamond light source. The sample was mounted and heated in the same way as for the in situ wide-angle X-ray scattering. The X-ray wavelength (0.161669 Å) was calibrated with Si standard sample (NIST, Gaithersburg, MD, USA). Data were processed using Fit2D software and pair distribution functions were produced using the PDFgetX3 software.

Infrared Spectroscopy: In situ infrared analysis were performed using a Fourier transform infrared spectrometer (Bruker Optik GmbH) equipped with a MCT-detector (32 scans, resolution 4 cm^{-1}). The sample was mounted and heated in the same way as for the in situ wide-angle X-ray scattering. Ex situ infrared spectra were collected using a Thermo Scientific Nicolet is5 FTIR spectrometer (ATR-Diamond mode) (32 scans, resolution 4 cm^{-1}).

Raman Spectroscopy: Raman spectra were collected using a confocal Raman microscope (α300; WITec) equipped with a CCD camera (DV401-BV; Andor), a Nikon objective (10×) and a 532 nm laser (40 accumulations, integration time 1 s). A high-resolution grating of 1800 g mm^{-1} was used and the spectral resolution was ≈1 cm^{-1}.

Amino Acid Analysis: Calcium carbonate powder with known weight was hydrolyzed in 6 N HCl containing 5% phenol by vacuum sealing and heating at 110 °C for 24 h. Hydrolyzed samples were then flash evaporated, resuspended in sample dilution buffer and run on a postcolumn ninhydrin-based amino acid analyzer (Sykam S433, Fürstenfeldbruck, Germany). AAA measurements were performed once for each sample.

X-Ray Photoelectron Spectroscopy: XPS investigations were in a PHI 5000C ESCA system (PerkinElmer, USA). A contaminant carbon (C 1s = 284.6 eV) was used as a reference to calibrate the binding energies.

Supporting Information

Supporting Information is available from the Wiley Online Library or from the author.

Acknowledgements

Conflict of Interest

The authors declare no conflict of interest.

Keywords

[1] a) S. Weiner, Y. Levi-Kalisman, S. Raz, L. Addadi, *Connect. Tissue Res.* **2003**, *44*, 214; b) J. Mahamid, A. Sharir, L. Addadi, S. Weiner, *Proc. Natl. Acad. Sci. USA* **2008**, *105*, 12748.

[2] Z. Zou, W. J. E. M. Habraken, G. Matveeva, A. C. S. Jensen, L. Bertinetti, M. A. Hood, C.-Y. Sun, P. U. P. A. Gilbert, I. Polishchuk, B. Pokroy, J. Mahamid, Y. Politi, S. Weiner, P. Werner, S. Bette, R. Dinnebier, U. Kolb, E. Zolotoyabko, P. Fratzl, *Science* **2019**, *363*, 396.

[3] a) F. Nudelman, H. H. Chen, H. A. Goldberg, S. Weiner, L. Addadi, *Faraday Discuss.* **2007**, *136*, 9; b) Y. Politi, T. Arad, E. Klein, S. Weiner, L. Addadi, *Science* **2004**, *306*, 1161.

[4] W. J. E. M. Habraken, A. Masic, L. Bertinetti, A. Al-Sawalmih, L. Glazer, S. Bentov, P. Fratzl, A. Sagi, B. Aichmayer, A. Berman, *J. Struct. Biol.* **2015**, *189*, 28.

[5] a) E. Loste, R. M. Wilson, R. Seshadri, F. C. Meldrum, *J. Cryst. Growth* **2003**, *254*, 206; b) Y. Politi, D. R. Batchelor, P. Zaslansky, B. F. Chmelka, J. C. Weaver, I. Sagi, S. Weiner, L. Addadi, *Chem. Mater.* **2010**, *22*, 161; c) J. D. Rodriguez-Blanco, S. Shaw, P. Bots, T. Roncal-Herrero, L. G. Benning, *J. Alloys Compd.* **2012**, *536*, S477; d) G. Magnabosco, A. M. M. Condorelli, R. Rosenberg, I. Polishchuk, B. Pokroy, D. Gebauer, H. Cölfen, G. Falini, *Chem. Commun.* **2019**, *55*, 12944; e) E. Seknazi, S. Kozachkevich, I. Polishchuk, N. Bianco Stein, J. Villanova, J.-P. Suuronen, C. Dejoie, P. Zaslansky, A. Katsman, B. Pokroy, *Nat. Commun.* **2019**, *10*, 4559; f) I. Polishchuk, A. A. Bracha, L. Bloch, D. Levy, S. Kozachkevich, Y. Etinger-Geller, Y. Kauffmann, M. Burghammer, C. Giacobbe, J. Villanova, G. Hendler, C.-Y. Sun, A. J. Giuffre, M. A. Marcus, L. Kundanati, P. Zaslansky, N. M. Pugno, P. U. P. A. Gilbert, A. Katsman, B. Pokroy, *Science* **2017**, *358*, 1294.

[6] a) I. Schmidt, E. Zolotoyabko, K. Lee, A. Gjardy, A. Berner, E. Lakin, P. Fratzl, W. Wagermaier, *Cryst. Res. Technol.* **2019**, *54*, 1900002; b) J. L. Littlewood, S. Shaw, C. L. Peacock, P. Bots, D. Trivedi, I. T. Burke, *Cryst. Growth Des.* **2017**, *17*, 1214.

[7] a) A. Gal, S. Weiner, L. Addadi, *J. Am. Chem. Soc.* **2010**, *132*, 13208; b) M. Kellermeier, E. Melero-García, F. Glaab, R. Klein, M. Drechsler, R. Rachel, J. M. García-Ruiz, W. Kunz, *J. Am. Chem. Soc.* **2010**, *132*, 17859; c) M. Kellermeier, D. Gebauer, E. Melero-García, M. Drechsler, Y. Talmon, L. Kienle, H. Cölfen, J. M. García-Ruiz, W. Kunz, *Adv. Funct. Mater.* **2012**, *22*, 4301.

[8] a) S. Bentov, S. Weil, L. Glazer, A. Sagi, A. Berman, *J. Struct. Biol.* **2010**, *171*, 207; b) S. Kababya, A. Gal, K. Kahil, S. Weiner, L. Addadi, A. Schmidt, *J. Am. Chem. Soc.* **2015**, *137*, 990; c) Y. Sugiura, K. Onuma, Y. Kimura, K. Tsukamoto, A. Yamazaki, *Am. Mineral.* **2013**, *98*, 262.

[9] a) L. B. Gower, *Chem. Rev.* **2008**, *108*, 4551; b) Y. Politi, J. Mahamid, H. Goldberg, S. Weiner, L. Addadi, *CrystEngComm* **2007**, *9*, 1171; c) D. J. Tobler, J. D. Rodriguez-Blanco, K. Dideriksen, N. Bovet, K. K. Sand, S. L. S. Stipp, *Adv. Funct. Mater.* **2015**, *25*, 3081.

[10] A. Rao, M. Drechsler, S. Schiller, M. Scheffner, D. Gebauer, H. Cölfen, *Adv. Funct. Mater.* **2018**, *28*, 1802063.

[11] Z. Zou, L. Bertinetti, Y. Politi, A. C. S. Jensen, S. Weiner, L. Addadi, P. Fratzl, W. J. E. M. Habraken, *Chem. Mater.* **2015**, *27*, 4237.

[12] a) Z. Zou, L. Bertinetti, Y. Politi, P. Fratzl, W. J. E. M. Habraken, *Small* **2017**, *13*, 11; b) A. Gal, K. Kahil, N. Vidavsky, R. T. DeVol, P. U. P. A. Gilbert, P. Fratzl, S. Weiner, L. Addadi, *Adv. Funct. Mater.* **2014**, *24*, 5420.

[13] a) E. Beniash, L. Addadi, S. Weiner, *J. Struct. Biol.* **1999**, *125*, 50; b) Y. Politi, R. A. Metzler, M. Abrecht, B. Gilbert, F. H. Wilt, I. Sagi, L. Addadi, S. Weiner, P. U. P. A. Gilbert, *Proc. Natl. Acad. Sci. USA* **2008**, *105*, 17362; c) A. Gal, S. Weiner, L. Addadi, *CrystEngComm* **2015**, *17*, 2606; d) A. Gal, W. Habraken, D. Gur, P. Fratzl, S. Weiner, L. Addadi, *Angew. Chem., Int. Ed.* **2013**, *52*, 4867.

[14] a) A. V. Radha, T. Z. Forbes, C. E. Killian, P. U. P. A. Gilbert, A. Navrotsky, *Proc. Natl. Acad. Sci. USA* **2010**, *107*, 16438; b) M. Faatz, F. Grohn, G. Wegner, *Adv. Mater.* **2004**, *16*, 996.

[15] a) M. P. Schmidt, A. J. Ilott, B. L. Phillips, R. J. Reeder, *Cryst. Growth Des.* **2014**, *14*, 938; b) N. Koga, Y. Z. Nakagoe, H. Tanaka, *Thermochim. Acta* **1998**, *318*, 239.

[16] a) J. Ihli, A. N. Kulak, F. C. Meldrum, *Chem. Commun.* **2013**, *49*, 3134; b) M. Albéric, L. Bertinetti, Z. Zou, P. Fratzl, W. Habraken, Y. Politi, *Adv. Sci.* **2018**, *5*, 1701000.

[17] J. Ihli, Y. Y. Kim, E. H. Noel, F. C. Meldrum, *Adv. Funct. Mater.* **2013**, *23*, 1575.

[18] J. Ihli, W. C. Wong, E. H. Noel, Y.-Y. Kim, A. N. Kulak, H. K. Christenson, M. J. Duer, F. C. Meldrum, *Nat. Commun.* **2014**, *5*, 3169.

[19] a) C. Rodriguez-Navarro, K. Kudlacz, O. Cizer, E. Ruiz-Agudo, *CrystEngComm* **2015**, *17*, 58; b) F. Konrad, F. Gallien, D. E. Gerard, M. Dietzel, *Cryst. Growth Des.* **2016**, *16*, 6310.

[20] Z. Zou, I. Polishchuk, L. Bertinetti, B. Pokroy, Y. Politi, P. Fratzl, W. J. E. M. Habraken, *J. Mater. Chem. B* **2018**, *6*, 449.

[21] a) D. Wang, L. M. Hamm, R. J. Bodnar, P. M. Dove, *J. Raman Spectrosc.* **2012**, *43*, 543; b) A. Fernandez-Martinez, B. Kalkan, S. M. Clark, G. A. Waychunas, *Angew. Chem., Int. Ed.* **2013**, *52*, 8354.

[22] a) S. Borukhin, L. Bloch, T. Radlauer, A. H. Hill, A. N. Fitch, B. Pokroy, *Adv. Funct. Mater.* **2012**, *22*, 4216; b) B. Pokroy, J. P. Quintana, E. N. Caspi, A. Berner, E. Zolotoyabko, *Nat. Mater.* **2004**, *3*, 900; c) B. Pokroy, A. Fitch, E. Zolotoyabko, *Adv. Mater.* **2006**, *18*, 2363; d) M. Albéric, E. N. Caspi, M. Bennet, W. Ajili, N. Nassif, T. Azaïs, A. Berner, P. Fratzl, E. Zolotoyabko, L. Bertinetti, Y. Politi, *Cryst. Growth Des.* **2018**, *18*, 2189.

[23] A. T. Patel, A. Pratap, *J. Therm. Anal. Calorim.* **2012**, *107*, 159.

[24] J. D. Rodriguez-Blanco, S. Shaw, L. G. Benning, *Nanoscale* **2011**, *3*, 265.

[25] A. C. S. Jensen, S. Imberti, S. F. Parker, E. Schneck, Y. Politi, P. Fratzl, L. Bertinetti, W. J. E. M. Habraken, *J. Phys. Chem. C* **2018**, *122*, 3591.

[26] H. Du, M. Steinacher, C. Borca, T. Huthwelker, A. Murello, F. Stellacci, E. Amstad, *J. Am. Chem. Soc.* **2018**, *140*, 14289.

[27] Z. Zyman, A. Goncharenko, *Process. Appl. Ceram.* **2017**, *11*, 147.

[28] A. Al-Sawalmih, C. Li, S. Siegel, P. Fratzl, O. Paris, *Adv. Mater.* **2009**, *21*, 4011.

[29] Y. Shibuta, K. Oguchi, T. Takaki, M. Ohno, *Sci. Rep.* **2015**, *5*, 13534.

[30] F. J. Millero, D. J. Hawke, *Mar. Chem.* **1992**, *40*, 19.

[31] a) A. C. S. Jensen, I. Rodriguez, W. J. E. M. Habraken, P. Fratzl, L. Bertinetti, *Phys. Chem. Chem. Phys.* **2018**, *20*, 19682; b) A. C. S. Jensen, S. Imberti, W. J. E. M. Habraken, L. Bertinetti, *J. Phys. Chem. C* **2020**, *124*, 6141.

[32] J. Rodríguez-Carvajal, *Newsl. Comm. Powder Diffr. IUCr* **2001**, *26*, 12.